

Exact theory of superconductivity from repulsion in narrow band systems

Valentin Crépel, Liang Fu

Massachusetts Institute of Technology, 77 Massachusetts Avenue, Cambridge, MA, USA

We introduce an analytically-controlled theory of superconductivity from repulsive interaction in narrow band systems, where pairing is induced by virtual composite excitations at high energy. A quantitative formula relating T_c to interaction strength and single-particle band gap is obtained, with maximum T_c reaching about 10% of the Fermi temperature. Our theory demonstrates a reliable and robust mechanism for strong coupling superconductivity, which enables unconventional pairing symmetry and filling-dependent gap structure.

Superconductivity in conventional metals results from an effective attraction between electrons mediated by the exchange of phonons [1, 2]. While this attraction is much weaker than the bare Coulomb repulsion [3], the latter is drastically renormalized downward by retardation effects [4]. Thanks to the vast difference between Fermi and Debye energy, the phonon-mediated attraction can overscreen the Coulomb repulsion to enable electron pairing and superconductivity [5]. On the other hand, this crucial retardation condition fails in systems with narrow bands or low carrier density. Yet superconductivity has been found in a growing number of materials in such strong-coupling regime. Two famous examples are (1) strontium titanate, the most dilute bulk superconductor with Fermi energy as small as 1meV [6]; (2) magic-angle graphene with a record-low density $n_{2D} \sim 10^{11} \text{cm}^{-2}$ and a very small bandwidth $\sim 10 \text{meV}$ [7–10]. Remarkably, the ratio of superconducting transition temperature T_c and Fermi temperature E_F/k_B far exceeds typical values, reaching as high as 0.01 in strontium titanate [6] and 0.1 in magic-angle graphene [8]. Finding electronic mechanisms for strong-coupling superconductivity in narrow band systems has long been a subject of great interest and challenge [11–14].

In this work, we introduce a simple two-band model of interacting spin-polarized fermions on a two-dimensional lattice to establish a general mechanism for unconventional superconductivity from strong repulsion. In our model, an insulating state occurs at the filling of $n = 1$ fermion per unit cell, and superconductivity emerges upon particle or hole doping. Based on a perturbative expansion around the atomic limit, we rigorously show that, despite the strong bare repulsion, a non-retarded short-range pairing interaction between doped fermions in the narrow band is generated by coupling to high-energy composite excitations. The resulting superconductor is unconventional by all standards. It has f -wave pairing symmetry and changes from having a full gap to point nodes above a critical doping. T_c is controlled by the bare interaction strength and the band gap, reaching as large as $T_c \sim 0.1E_F/k_B$ when they are of comparable magnitude. Our theory is analytically controlled by a small coupling constant that emerges in the narrow band limit. Our work demonstrates a reliable and robust mechanism for unconventional superconductivity from repulsion in narrow band systems.

Our model is broadly inspired by a recent work by Slagle and one of us [15], who proposed a mechanism for pairing from purely *classical* electrostatic repulsion in a doped charge transfer insulator. The essential ingredient there is a charge- $2e$ excitation dubbed “trimer”, which is a composite object consisting of two doped electrons tightly bound to a dipole. Interestingly, for certain extended Coulomb repulsion, a trimer is energetically more favored than two separate electrons. Under appropriate conditions, the presence of preformed trimers can lead to Wigner crystal or superconducting ground states at small doping.

While we also start with the problem of doping an insulator, our work differs fundamentally from Ref. [15]. We find superconductivity without invoking trimers or any preformed pairs at low energy. Instead, pairing arises from correlated *quantum* hopping of doped fermions induced by *virtual* composite excitations at high energy. We demonstrate this novel mechanism by introducing and solving the simplest model of spin-polarized fermions interacting on a bipartite lattice. Last but not the least, our solution reveals distinct superconducting states at different ranges of doping and provides a quantitative formula for T_c in terms of microscopic parameters.

We consider spin-polarized fermions on the honeycomb lattice with repulsive interactions, described by the Hamiltonian

$$\begin{aligned}\mathcal{H} &= \mathcal{H}_0 + \mathcal{H}_t, \\ \mathcal{H}_0 &= V \sum_{\langle r, r' \rangle} n_r n_{r'} + \Delta \sum_{r \in B} n_r, \\ \mathcal{H}_t &= -t \sum_{\langle r, r' \rangle} (c_r^\dagger c_{r'} + hc). \end{aligned} \quad (1)$$

where \mathcal{H}_0 contains the nearest-neighbor interaction – the dominant interaction for spin-polarized fermions on a lattice – and the sublattice potential difference between the two inequivalent A and B sites, while \mathcal{H}_t describes tunneling between adjacent sites. Despite the simplicity of our model, in this work we unveil its remarkably rich phase diagram as a function of filling and interaction strength. We shall derive the low-energy properties of the system with a fully-controlled perturbative expansion in the narrow-band limit $t \ll \Delta$, which we further complement with field-theoretic analysis and extensive exact diagonalization (ED) studies.

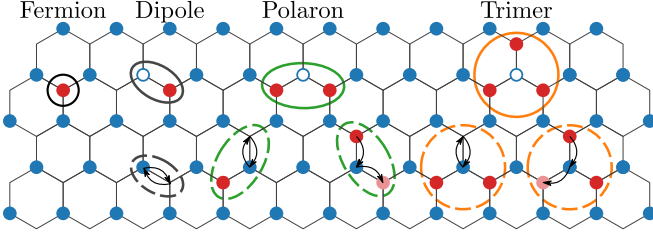


FIG. 1. Low energy fermion added above the $n = 1$ insulating background live on the B lattice. Excitations above this f -band are dipoles, polarons and trimers (solid circles), whose virtual occupation leads to the effective model Eq. (2) (dashed circles).

In the strong coupling limit, the ground state of \mathcal{H} at $n = 1$ is an insulator with all A sites occupied and all B sites empty, as shown in Fig. 1. Its insulating property is ensured by the large gap $E_D = 2V + \Delta$, which corresponds to the energy necessary to transfer an electron from an A site to B , or equivalently, creating a dipole. The inclusion of tunneling, small compared to E_D , slightly decreases the charge transfer gap without any significant change to the insulating ground state.

Since \mathcal{H} is invariant under particle-hole transformation $c_A \rightarrow c_A^\dagger, c_B \rightarrow -c_B^\dagger$ combined with spatial inversion that interchanges the two sublattices, it suffices to consider $n > 1$ filling below. At finite doping $n = 1 + \delta$ ($\delta > 0$), low energy configurations of the system remain with all A sites occupied in order to avoid the large charge transfer gap. Due to Pauli exclusion principle, the δ additional fermions must live on the B lattice, and in the limit $t = 0$, form a highly degenerate manifold with an energy $E_f = \Delta + 3V$ per doped charge that we refer to as f -band.

Besides these fermions on B sites, there exist various types of composite excitations at higher energy, which involve holes on A sites, as depicted in Fig. 1. For example, a B -fermion can bind with a neighboring dipole to form a charge- e Fermi polaron, which has energy $E_P = E_f + V + \Delta$. More interesting is the charge- $2e$ trimer, which consists of three neighboring B -fermions surrounding a hole on the center A site. It can also be viewed as two neighboring B -fermions tightly bound to a dipole. A trimer costs energy $E_T = 2E_f + \Delta$, which is greater than the energy of two separate B -fermions by Δ . These composite excitations – dipoles, polarons and trimers – are hereafter collectively referred to as charge-transfer complex.

In the presence of small quantum tunneling $t \ll \Delta$, doped carriers in the f -band constitute the only low-energy excitations in our system. They virtually couple to charge-transfer complex at high energy. This coupling results in a narrow dispersive f -band of doped carriers and induces short-range interactions between them. Remarkably, we shall show that the induced interaction leads to pairing within the f -band. To that purpose, we analytically carry out a Schrieffer-Wolff transformation $\mathcal{H}' = e^{iS} \mathcal{H} e^{-iS}$ to decouple the f -band from high energy

degrees of freedom [16, 17]. As detailed in App. A, this procedure accounts for all possible virtual processes (see Fig. 1), and leads to the following effective Hamiltonian for doped fermions, which is *exact* to second order in t/Δ and at any f -band filling:

$$\begin{aligned} \mathcal{H}' = & \sum_{\langle i,j \rangle} t_f (f_i^\dagger f_j + hc) + V_f n_i n_j \\ & + \sum_{(ijk) \in \Delta} \lambda (f_i^\dagger n_j f_k + P_{ijk}) + U_3 n_i n_j n_k. \end{aligned} \quad (2)$$

The f_i fermionic operators denote the doped fermions on the triangular B -lattice, and their vacuum is the $n = 1$ insulating state described above. The sums labeled by $\langle i,j \rangle$ and $(i,j,k) \in \Delta$ respectively run over all bonds and all *upper* triangles of the B -lattice, while P_{ijk} stands for the inclusion of $f_i^\dagger n_j f_k$ with all possible permutations of the indices i, j and k .

The effective Hamiltonian \mathcal{H}' for doped fermions consists of single-particle tunneling, correlated (density-dependent) tunneling, two-body and three-body density interactions. Their origins can be understood as follows. The tunneling from k to i in the upper triangle (ijk) arises from two consecutive hopping processes. The virtual intermediate state involved is either a polaron or a trimer, depending on the occupation of site j (see Fig. 1). The resulting tunneling amplitude is thus $t^2[(1 - n_j)/(E_P - E_f) + n_j/(E_T - 2E_f)]$, from which the expression of t_f and λ are derived:

$$t_f = \frac{t^2}{\Delta + V}, \quad (3a)$$

$$\lambda = \frac{t^2}{\Delta} - \frac{t^2}{\Delta + V}. \quad (3b)$$

The interaction coefficients V_f and U_3 come from processes where an A fermion hops back and forth between neighboring sites (see Fig. 1). For example, V_f measures the difference of energy between two neighboring doped charges on B sites and two well-separated ones. The former configuration can couple to a trimer state whereas the latter cannot, thus leading to an attraction $-t^2/\Delta$. Accounting for all processes, we find

$$V_f = -\frac{t^2}{\Delta} + \frac{4t^2}{\Delta + V} - \frac{3t^2}{\Delta + 2V}, \quad (3c)$$

$$U_3 = \frac{3t^2}{\Delta} - \frac{6t^2}{\Delta + V} + \frac{3t^2}{\Delta + 2V}. \quad (3d)$$

In Eq. (3a-d), the denominators Δ , $\Delta + V$ and $\Delta + 2V$ are the energy costs of intermediate states involving trimer, polaron and dipole respectively. Importantly, higher-order corrections to the effective Hamiltonian \mathcal{H}' are small provided that the narrow band condition $t \ll \Delta$ is satisfied, regardless of interaction strength V .

At small $V \ll \Delta$, the effective interactions in the f -band are found to be $V_f^0 = 2(t/\Delta)^2 V$, $\lambda^0 = (t/\Delta)^2 V$ and

$U_3^0 = 0$ to first order in V/Δ . These values simply correspond to the projection of the bare repulsion V into the f -band, whose wavefunctions have small amplitudes $\sim t/\Delta$ on A sites. As V increases, interband mixing quickly becomes important and our exact results (3a-d) reveals a dramatic departure of the “dressed” interaction from the projected interaction. As opposed to the projected interactions, V_f starts to decrease at $V \approx 0.29\Delta$ and changes sign from repulsive to attractive at $V = \Delta$. Similarly, λ and U_3 show manifest deviations from the projected estimates for $V > 0.1\Delta$, and saturate at large V/Δ (see App. A). In the rest of this work, we shall mainly consider the case $V < \Delta$, where the induced V_f, λ, U_3 turn out to be positive and small compared to the single-particle bandwidth $W = 9t_f$.

To reveal the tendency towards pairing, we study the formation of two-particle bound states, the analog of “Cooper problem” in a doped insulator. Pair formation is evidenced by the positivity of the pair binding energy

$$\begin{aligned}\varepsilon_b &= 2[E(1) - E(0)] - [E(2) - E(0)] \\ &= 2E(1) - E(2) - E(0),\end{aligned}\quad (4)$$

with $E(m)$ the ground state energy of a system with m charges added above $n = 1$ filling. As detailed in App. B, we analytically solve the lattice Hamiltonian Eq. (2) in the case of two doped fermions and obtain ε_b as a function of V/Δ , shown in Fig. 2. It is found positive in the entire range V/Δ . This result shows an effective pairing interaction between low-energy fermions. It is worth noting that the two-particle bound states cannot be captured by the projected interaction $V_f^0 = 2\lambda^0$, which proves that pairing is induced by virtual interband excitations. We further confirm the formation of pairs in the original model Eq. (1) with ED, see App. E. Interestingly, pairs are already present for $V < \Delta$ despite a repulsive induced nearest neighbor interaction ($V_f > 0$). This highlights the essential role of correlated hopping λ in the effective model for pairing.

The two-particle bound state we found has zero total momentum, is symmetric under three-fold rotation, and changes sign under reflection that flips one of the primitive vectors \mathbf{a}_j , *i.e.* it has f -wave pairing symmetry. The size of the bound state shrinks with increasing V/Δ , as shown in the inset of Fig. 2 for $V/\Delta = 0.5$ and 100. At small V/Δ , the pair wavefunction is highly extended over many lattice sites, while in the opposite limit $V/\Delta \rightarrow \infty$, two nearest-neighbor fermions form the most tightly bound pair “resonating” within a single upper triangle (see App. B). Our solution of the two-particle problem suggests a crossover between BCS and BEC states at small particle density, tuned by V/Δ .

We now extend our analysis to finite, but small, doping concentrations δ above $n = 1$. In this regime, the physics of dilute doped fermions is governed by long-wavelength properties that transcend the details on the lattice scale. This motivates us to derive a low-energy theory by taking the continuum limit of the lattice Hamiltonian. This is achieved by rewriting the lattice Hamiltonian in terms of

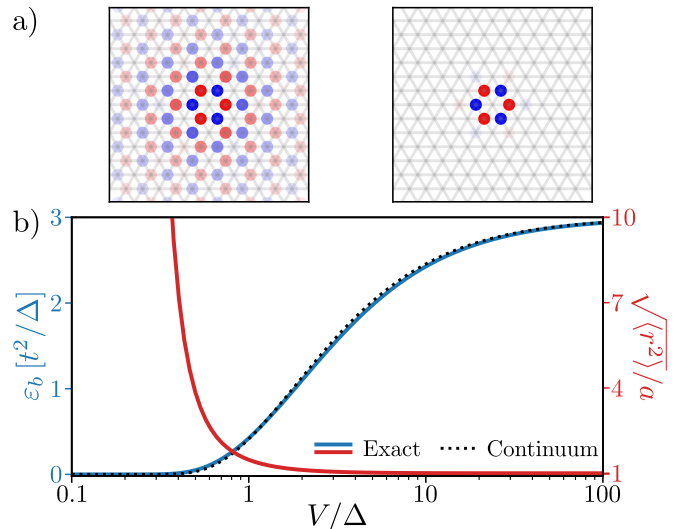


FIG. 2. a) The transition from weakly to tightly bound pairs, depicted for $V/\Delta = 0.5$ (left) and 10 (right), constitutes a probe of the BCS-BEC crossover at low doping. b) Pair binding energy ε_b and bound state size as a function of V/Δ from the exact solution of the two fermion problem. The prediction of the continuum model (dashed) perfectly match the full-fledged lattice calculation, a stringent test of our derivation.

fermionic fields in momentum space and retaining only modes near the bottom of the f -band. Importantly, the band dispersion $\varepsilon(\mathbf{k}) = 2t_f \sum_{j=1}^3 \cos(\mathbf{k} \cdot \mathbf{a}_j)$, with $t_f > 0$, has two degenerate minima located at the $\pm \mathbf{K}$ points of the Brillouin zone. Therefore, low-energy degrees of freedom are described by two long-wavelength fermionic fields $\psi_\tau(\mathbf{q}) = f(\tau \mathbf{K} + \mathbf{q})$ with $qa \ll 1$, distinguished by the valley index $\tau = \pm$. In App. C, we find the following continuum Hamiltonian for ψ_τ :

$$\tilde{\mathcal{H}} = \int d\mathbf{x} \sum_{\tau=\pm} \psi_\tau^\dagger \left[\frac{-\nabla^2}{2m} \right] \psi_\tau + g \psi_+^\dagger \psi_+ \psi_-^\dagger \psi_-, \quad (5)$$

where the effective mass and interaction strength are entirely determined from the lattice parameters:

$$\begin{aligned}m &= 2/(3t_f a^2), \\ g &= 6a^2(V_f - 2\lambda) < 0.\end{aligned}\quad (6)$$

The resulting quantum field theory describes a *two-flavor* fermion gas in the continuum with *attractive* contact interaction. The two flavors correspond to the valley degree of freedom associated with the underlying lattice, from which the field theory is derived. This theory is asymptotically exact in the low doping limit where s -wave scattering between fermions of opposite valleys is the dominant interaction.

This attractive interaction leads to the formation valley-singlet two-particle bound states, which exactly correspond to the f -wave pairs observed on the lattice (see Fig. 2). Indeed, the pair amplitude $f_{+\mathbf{K}} f_{-\mathbf{K}}$ is odd

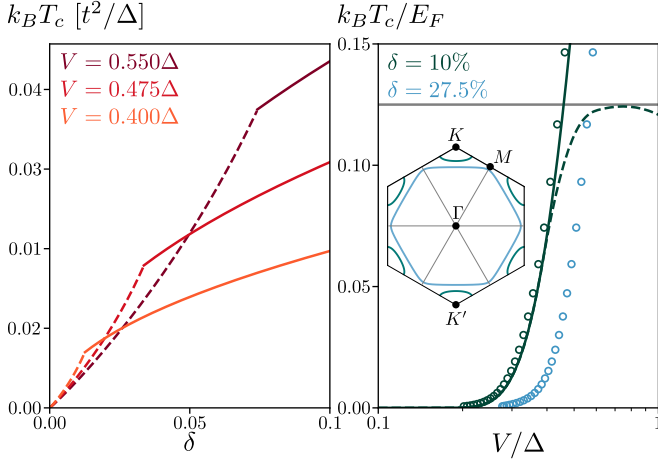


FIG. 3. Critical temperature of the continuum model in the exact BCS (solid, Eq. (8)) and BEC (dashed) limits, as a function of doping and V/Δ . A gray horizontal line highlights the bound $k_B T_c < E_F/8$. The self-consistent lattice mean-field solutions (dots) agree with the continuum theory for small doping, but differ when the $\pm K$ pockets merge (inset).

under the reflection that interchanges the two valleys. To verify the validity of our continuum model, we calculate the two-particle binding energy ε_b in the field theory, and using the parameters m and g given by Eq. (6) and (3), compare it with the exact solution of the lattice model. The expression for ε_b is

$$\frac{\varepsilon_b}{\varepsilon_{uv}} = \left[e^{1/g_0} - 1 \right]^{-1},$$

$$g_0 = \frac{9}{\pi} \frac{2\lambda - V_f}{W} = \frac{6}{\pi} \frac{V^2}{\Delta(\Delta + 2V)}, \quad (7)$$

with $\varepsilon_{uv} = \pi W/9$ an energy cutoff that we fix with the exact binding energy at $V \rightarrow \infty$ (see App. C). The exponent g_0 in Eq. (7), defined by the ratio of effective pairing interaction g and the bandwidth, only depends on the ratio V/Δ in the narrow band regime $t \ll \Delta$. Remarkably, a perfect agreement between continuum theory and lattice model is found at all values of V/Δ (see Fig. 2). This proves the accuracy of our mapping from lattice model to continuum theory.

The attractive Fermi gas in two dimensions is known to be superconducting at low temperature and exhibits a BCS-BEC crossover as the ratio between pair binding and Fermi energies changes from small to large values [18–20]. In the region of weakly bound pairs $\varepsilon_b \ll E_F$, the critical temperature is given by $k_B T_c = e^{\gamma-1} \sqrt{2E_F \varepsilon_b}/\pi$ with $\gamma \simeq 0.577$ Euler’s constant [21–23]. From the expression for binding energy Eq. (7), we derive a formula for T_c in our model:

$$k_B T_c = e^{\gamma-1} \sqrt{\frac{2E_F W}{9\pi}} e^{-1/(2g_0)}. \quad (8)$$

On the other side of the crossover $\varepsilon_b \gg E_F$, the physics depends on the interaction between the bosonic pairs.

When these bosons repel, the system exhibits a BKT transition toward a BEC at low temperature [24], while it collapses if bosons attract [25, 26]. Between the extreme BCS and BEC limits, the critical temperature satisfies the very general bound $k_B T_c \leq E_F/8$ [27], which limits the largest achievable T_c .

The BCS-BEC crossover of the two-dimensional Fermi gas can be achieved by tuning either carrier density or the interaction strength g_0 , which is controlled by V/Δ in our model. We plot in Fig. 3 the critical temperature T_c as a function of doping concentration δ and V/Δ . At very low doping where $E_F < \varepsilon_b$, the system lies in the BEC regime and T_c increases rapidly with δ . At some critical concentration, the system undergoes the BEC-BCS crossover and finally follows Eq. (8).

From the expression of g_0 (Eq. (7)), we infer the critical temperature as a function of V/Δ . It is worth emphasizing that our exact BCS formula Eq. (8) applies provided that the dimensionless coupling constant g_0 is small, even when the bare repulsion V far exceeds the bandwidth W . This is because doped fermions at the conduction band bottom $\pm K$ reside entirely on B sublattice, and therefore avoid the direct nearest-neighbor repulsion V . In the weak-coupling regime $V \ll \Delta$, the attraction $g_0 \propto (V/\Delta)^2$ between low-energy carriers is induced by virtual interband particle-hole pairs or excitons, and leads to exponentially small T_c . Most importantly however, our expression of g_0 is nonperturbative in V and remains exact at $V \sim \Delta \gg W$, where strong-coupling superconductivity and maximum T_c are attained. For instance, at doping $\delta = 0.1$, T_c reaches $0.1E_F \simeq 0.032t^2/\Delta$ around $V = 0.43\Delta$, which is about 0.5% of the quasi-particle bandwidth $W = 9t_f \simeq 6.3t^2/\Delta$. More generally, Eq. (8) can safely be applied for $V < 0.7\Delta$, since $\exp(1/g_0) > 10$ and $\varepsilon_b \lesssim E_F/2$ [19].

We support the emergence of superconductivity with evidence from ED on finite size lattices. While the original model Eq. (1) exhibits positive ε_b (see App. E), we focus on the effective model Eq. (2) which allows to reach larger system sizes. First, the superfluid behavior of the system is probed by the charge stiffness [28]

$$D = \frac{1}{16\pi^2} \frac{L_1}{L_2} \left. \frac{\partial^2 E(N, \phi)}{\partial \phi^2} \right|_{\phi=0} \quad (9)$$

at doping $\delta = N/(L_1 \times L_2)$, with N the number of doped fermions and (L_1, L_2) the number of sites along the two basis vectors of the triangular lattice. D measures the sensitivity of the ground state energy $E(N, \phi)$ to twisted boundary conditions $\psi_{r+L_1} = e^{2i\pi\phi}\psi_r$. A positive value of $D > 0$ in the thermodynamic limit implies dissipationless charge transport and gives a direct signature of the Meissner effect [29]. In the range of parameters considered, our system clearly exhibits (with small finite-size effect) the $h/2e$ flux periodicity of superconductors [30] and shows positive D (see Fig. 4a-b), which proves superconductivity in the ground state. The charge stiffness of a BCS superconductor with a parabolic dispersion relation is known exactly: $D = E_F/4\pi$ [27]. Our results

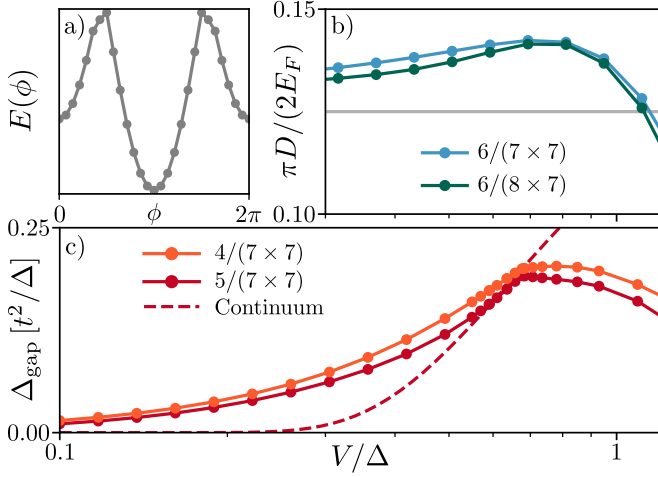


FIG. 4. a) The ground state energy exhibits the characteristic flux dependence of a superconductor, as shown here for $V = \Delta$ and 6 particles on a 8×6 lattice. b) The charge stiffness divided by the Fermi energy is constant in the BCS limit, reaching $1/8$ for small doping (gray). b) Superconducting gap as a function of V/Δ for different doping concentrations. It follows the continuum prediction (dashed) up to $V/\Delta \simeq 0.7$.

for $V < \Delta$ are correctly captured by this prediction, especially at low doping concentrations where fermions live close to the band minima.

To demonstrate the strong-coupling nature of the superconducting state, we consider the superconducting gap

$$\Delta_{\text{gap}} = \frac{(-1)^N}{2} [E(N+1) + E(N-1) - 2E(N)] . \quad (10)$$

Our continuum theory Eq. (5) predicts $\Delta_{\text{gap}} = \sqrt{2E_F \varepsilon_b}$ up to $V \sim \Delta$. This leads to a ratio of the gap and critical temperature $\Delta_{\text{gap}}/k_B T_c = \pi e^{1-\gamma} \simeq 4.796$, which is much larger than the universal value 1.764 in BCS theory for weak-coupling superconductors [31]. This is because the phonon-induced retarded attraction in conventional metals is limited to electrons within a Debye energy from the Fermi surface, whereas in our theory the induced pairing interaction is instantaneous on the time scale of inverse bandwidth (\hbar/W), so that all carriers in the narrow band are subject to the pairing interaction.

Our numerical results for $\delta \simeq 0.1$, shown in Fig. 4b, agree with the mean field prediction up to $V/\Delta = 0.7$, where the gap extracted from ED reaches as large as $\Delta_{\text{gap}} = 0.84E_F$. This allows the system to reach critical temperature of $0.1E_F$, as described above. For $V < 0.3\Delta$, the finite lattice size in ED study forbids the bound state to fully form (see Fig. 2), resulting in an overestimate of the superconducting gap compared to the continuum theory prediction.

In addition to the BCS-BEC superconductivity at low density, our model shows very rich physics at higher doping concentrations, where lattice effects become important. By performing mean-field calculation on the model

Eq. (2), we find f -wave pairing for doping $\delta < 1/3$ (see App. F). The corresponding critical temperatures, shown in Fig. 3, are calculated with the linearized gap equation

$$\frac{1}{\alpha} = \frac{1}{N_s} \sum_{\mathbf{q}} \frac{[\sum_j \sin(\mathbf{q} \cdot \mathbf{a}_j)]^2}{|\xi_{\mathbf{k}}|} \tanh\left(\frac{|\xi_{\mathbf{k}}|}{2k_B T_c}\right) \quad (11)$$

with $\xi_{\mathbf{k}} = \varepsilon(\mathbf{k}) - \mu$ and $\alpha = 2\lambda - V_f - (2\beta + \delta)U_3$, where $\beta = (3N_s)^{-1} \sum_{\mathbf{q}} f_{\text{FD}}(\xi_{\mathbf{k}}) \sum_j \cos(\mathbf{q} \cdot \mathbf{a}_j)$ originates from three-body interactions. Here, N_s denotes the total number of sites, and the chemical potential is fixed by $\delta = N_s^{-1} \sum_{\mathbf{q}} f_{\text{FD}}(\xi_{\mathbf{k}})$, with f_{FD} the Fermi-Dirac distribution.

At low doping, the f -wave superconducting state has a full pairing gap and its T_c obtained from lattice model calculation agrees well with our previous result based on continuum theory. Interestingly, at higher doping concentration $\delta > \delta_c \approx 1/4$, the gap vanishes at 6 nodes on the Fermi surface along ΓM direction, where the f -wave gap function vanishes. This change in gap structure is due to the change of Fermi surface topology across the van Hove singularity, where the two pockets around $\pm K$ merge into a single Fermi surface enclosing the Γ point (see Fig. 3).

The above conclusions are confirmed by our ED study, which shows clear evidence of nodal superconductivity at $\frac{1}{4} < \delta \leq \frac{1}{3}$. We also find that the superconducting state is remarkably robust against longer range bare repulsion. These numerical results can respectively be found in App. G and D. Finally, the ground state at sufficiently large V/Δ is found to be non-superconducting (see App. H), which we leave for further study in a separate work.

Our work opens a new route to unconventional superconductivity in atomic Fermi gas and electron systems. Encouragingly, optical lattice with honeycomb geometry and tunable band gap have already been realized [32, 33]. Many recent advances in dipolar or Rydberg atom systems with longer-range interactions [34, 35] have enabled the implementation of one-dimensional $t - V$ Hamiltonian [36], and hold great promise for the realization of our model in near future.

Our mechanism for strong-coupling superconductivity mediated by charge-transfer complex, or interband excitations, may also shed insight on graphene-based moiré superlattices, where the small bandwidth and high $k_B T_c/E_F$ ratio (up to ~ 0.1) place important constraints on viable theories. It will be interesting to develop accurate low-energy models for these systems and analyze superconductivity in the narrow band limit as exemplified in our work. In this regard, we note that correlated hopping and direct repulsion also appear in effective Hamiltonian for narrow bands in twisted bilayer graphene [37–39]. Our theory suggests that renormalization by virtual interband excitations is necessary to obtain strong-coupling superconductivity. Moreover, our simple model may be relevant to twisted double bilayer graphene [40] and trilayer graphene-boron nitride heterostructures [41], where signs of spin-polarized superconductivity has been

reported [42, 43]. We leave to future work the extension of our theory to spinful systems and its application to various strongly-correlated materials.

Acknowledgments. This work was supported by DOE

Office of Basic Energy Sciences, Division of Materials Sciences and Engineering under Award DE-SC0019275. LF was supported in part by a Simons Investigator Award from the Simons Foundation.

-
- [1] John Bardeen, Leon N Cooper, and John Robert Schrieffer, “Theory of superconductivity,” *Physical review* **108**, 1175 (1957).
 - [2] Herbert Fröhlich, “Theory of the superconducting state. i. the ground state at the absolute zero of temperature,” *Physical Review* **79**, 845 (1950).
 - [3] John Bardeen and David Pines, “Electron-phonon interaction in metals,” *Physical Review* **99**, 1140 (1955).
 - [4] P Morel and PW Anderson, “Calculation of the superconducting state parameters with retarded electron-phonon interaction,” *Physical Review* **125**, 1263 (1962).
 - [5] NN Bogoljubov, Vladimir Veniaminovic Tolmachov, and DV Širkov, “A new method in the theory of superconductivity,” *Fortschritte der physik* **6**, 605–682 (1958).
 - [6] Xiao Lin, Zengwei Zhu, Benoît Fauqué, and Kamran Behnia, “Fermi surface of the most dilute superconductor,” *Phys. Rev. X* **3**, 021002 (2013).
 - [7] Yuan Cao, Valla Fatemi, Shiang Fang, Kenji Watanabe, Takashi Taniguchi, Efthimios Kaxiras, and Pablo Jarillo-Herrero, “Unconventional superconductivity in magic-angle graphene superlattices,” *Nature* **556**, 43–50 (2018).
 - [8] Xiaobo Lu, Petr Stepanov, Wei Yang, Ming Xie, Mohammed Ali Aamir, Ipsita Das, Carles Urgell, Kenji Watanabe, Takashi Taniguchi, Guangyu Zhang, *et al.*, “Superconductors, orbital magnets and correlated states in magic-angle bilayer graphene,” *Nature* **574**, 653–657 (2019).
 - [9] Jeong Min Park, Yuan Cao, Kenji Watanabe, Takashi Taniguchi, and Pablo Jarillo-Herrero, “Tunable phase boundaries and ultra-strong coupling superconductivity in mirror symmetric magic-angle trilayer graphene,” *arXiv preprint arXiv:2012.01434* (2020).
 - [10] Zeyu Hao, AM Zimmerman, Patrick Ledwith, Eslam Khalaf, Danial Haie Najafabadi, Kenji Watanabe, Takashi Taniguchi, Ashvin Vishwanath, and Philip Kim, “Electric field tunable unconventional superconductivity in alternating twist magic-angle trilayer graphene,” *arXiv preprint arXiv:2012.02773* (2020).
 - [11] Jonathan Ruhman and Patrick A Lee, “Superconductivity at very low density: The case of strontium titanate,” *Physical Review B* **94**, 224515 (2016).
 - [12] Mingpu Qin, Chia-Min Chung, Hao Shi, Ettore Vitali, Claudius Hubig, Ulrich Schollwöck, Steven R White, Shiwei Zhang, *et al.*, “Absence of superconductivity in the pure two-dimensional hubbard model,” *Physical Review X* **10**, 031016 (2020).
 - [13] S Raghu, SA Kivelson, and DJ Scalapino, “Superconductivity in the repulsive hubbard model: An asymptotically exact weak-coupling solution,” *Physical Review B* **81**, 224505 (2010).
 - [14] Saurabh Maiti and Andrey V Chubukov, “Superconductivity from repulsive interaction,” in *AIP Conference Proceedings*, Vol. 1550 (American Institute of Physics, 2013) pp. 3–73.
 - [15] Kevin Slagle and Liang Fu, “Charge transfer excitations, pair density waves, and superconductivity in moiré materials,” *arXiv preprint arXiv:2003.13690* (2020).
 - [16] John R Schrieffer and Peter A Wolff, “Relation between the anderson and kondo hamiltonians,” *Physical Review* **149**, 491 (1966).
 - [17] Allan H MacDonald, SM Girvin, and D t Yoshioka, “t/u expansion for the hubbard model,” *Physical Review B* **37**, 9753 (1988).
 - [18] Mohit Randeria, Ji-Min Duan, and Lih-Yir Shieh, “Bound states, cooper pairing, and bose condensation in two dimensions,” *Physical review letters* **62**, 981 (1989).
 - [19] Gianluca Bertainia and S Giorgini, “Bcs-bec crossover in a two-dimensional fermi gas,” *Physical review letters* **106**, 110403 (2011).
 - [20] Meera M Parish, “The bcs-bec crossover,” in *Quantum Gas Experiments: Exploring Many-Body States* (World Scientific, 2015) pp. 179–197.
 - [21] Kazumasa Miyake, “Fermi liquid theory of dilute submonolayer 3he on thin 4he ii film: dimer bound state and cooper pairs,” *Progress of theoretical physics* **69**, 1794–1797 (1983).
 - [22] LP Gor’kov and TK Melik-Barkhudarov, “Contribution to the theory of superfluidity in an imperfect fermi gas,” *Sov. Phys. JETP* **13**, 1018 (1961).
 - [23] DS Petrov, MA Baranov, and GV Shlyapnikov, “Superfluid transition in quasi-two-dimensional fermi gases,” *Physical Review A* **67**, 031601 (2003).
 - [24] Daniel S Fisher and PC Hohenberg, “Dilute bose gas in two dimensions,” *Physical Review B* **37**, 4936 (1988).
 - [25] IPA Ruprecht, MJ Holland, K Burnett, and Mark Edwards, “Time-dependent solution of the nonlinear schrödinger equation for bose-condensed trapped neutral atoms,” *Physical Review A* **51**, 4704 (1995).
 - [26] Jacob L Roberts, Neil R Claussen, Simon L Cornish, Elizabeth A Donley, Eric A Cornell, and Carl E Wieman, “Controlled collapse of a bose-einstein condensate,” *Physical Review Letters* **86**, 4211 (2001).
 - [27] Tamaghna Hazra, Nishchal Verma, and Mohit Randeria, “Bounds on the superconducting transition temperature: Applications to twisted bilayer graphene and cold atoms,” *Physical Review X* **9**, 031049 (2019).
 - [28] Walter Kohn, “Theory of the insulating state,” *Phys. Rev.* **133**, A171–A181 (1964).
 - [29] Douglas J Scalapino, Steven R White, and Shoucheng Zhang, “Insulator, metal, or superconductor: The criteria,” *Physical Review B* **47**, 7995 (1993).
 - [30] F. Loder, A. P. Kampf, and T. Kopp, “Crossover from hc/e to $hc/2e$ current oscillations in rings of s-wave superconductors,” *Phys. Rev. B* **78**, 174526 (2008).
 - [31] J.R. Schrieffer, *Theory Of Superconductivity* (CRC Press, 2018).
 - [32] Thomas Uehlinger, Gregor Jotzu, Michael Messer, Daniel Greif, Walter Hofstetter, Ulf Bissbort, and Tilman Esslinger, “Artificial graphene with tunable interactions,” *Physical review letters* **111**, 185307 (2013).

- [33] Nick Fläschner, BS Rem, M Tarnowski, D Vogel, D-S Lühmann, K Sengstock, and Christof Weitenberg, “Experimental reconstruction of the berry curvature in a floquet bloch band,” *Science* **352**, 1091–1094 (2016).
- [34] S Baier, D Petter, JH Becher, A Patscheider, G Natale, L Chomaz, MJ Mark, and F Ferlaino, “Realization of a strongly interacting fermi gas of dipolar atoms,” *Physical review letters* **121**, 093602 (2018).
- [35] Mingwu Lu, Nathaniel Q Burdick, and Benjamin L Lev, “Quantum degenerate dipolar fermi gas,” *Physical Review Letters* **108**, 215301 (2012).
- [36] Elmer Guardado-Sanchez, Benjamin Spar, Peter Schauss, Ron Belyansky, Jeremy T Young, Przemyslaw Bienias, Alexey V Gorshkov, Thomas Iadecola, and Waseem S Bakr, “Quench dynamics of a fermi gas with strong long-range interactions,” *arXiv preprint arXiv:2010.05871* (2020).
- [37] Francisco Guinea and Niels R Walet, “Electrostatic effects, band distortions, and superconductivity in twisted graphene bilayers,” *Proceedings of the National Academy of Sciences* **115**, 13174–13179 (2018).
- [38] Jian Kang and Oskar Vafeek, “Strong coupling phases of partially filled twisted bilayer graphene narrow bands,” *Phys. Rev. Lett.* **122**, 246401 (2019).
- [39] Mikito Koshino, Noah F. Q. Yuan, Takashi Koretsune, Masayuki Ochi, Kazuhiko Kuroki, and Liang Fu, “Maximally localized wannier orbitals and the extended hubbard model for twisted bilayer graphene,” *Phys. Rev. X* **8**, 031087 (2018).
- [40] Xiaomeng Liu, Zeyu Hao, Eslam Khalaf, Jong Yeon Lee, Yuval Ronen, Hyobin Yoo, Danial Haei Najafabadi, Kenji Watanabe, Takashi Taniguchi, Ashvin Vishwanath, *et al.*, “Tunable spin-polarized correlated states in twisted double bilayer graphene,” *Nature* **583**, 221–225 (2020).
- [41] Guorui Chen, Aaron L Sharpe, Patrick Gallagher, Ilan T Rosen, Eli J Fox, Lili Jiang, Bosai Lyu, Hongyuan Li, Kenji Watanabe, Takashi Taniguchi, *et al.*, “Signatures of tunable superconductivity in a trilayer graphene moiré superlattice,” *Nature* **572**, 215–219 (2019).
- [42] Jong Yeon Lee, Eslam Khalaf, Shang Liu, Xiaomeng Liu, Zeyu Hao, Philip Kim, and Ashvin Vishwanath, “Theory of correlated insulating behaviour and spin-triplet superconductivity in twisted double bilayer graphene,” *Nature communications* **10**, 1–10 (2019).
- [43] Eyal Cornfeld, Mark S Rudner, and Erez Berg, “Spin-polarized superconductivity: order parameter topology, current dissipation, and multiple-period josephson effect,” *arXiv e-prints*, arXiv:2006 (2020).
- [44] Julien Vidal, Benoit Douçot, Rémy Mosseri, and Patrick Butaud, “Interaction induced delocalization for two particles in a periodic potential,” *Physical review letters* **85**, 3906 (2000).
- [45] Jesper Levinsen and Meera M Parish, “Strongly interacting two-dimensional fermi gases,” in *Annual review of cold atoms and molecules* (World Scientific, 2015) pp. 1–75.

Appendix A: Schrieffer-Wolff Transformation

In this appendix, we derive effective model Eq. 2 with a Schrieffer-Wolff transformation. This effective Hamiltonian is exact up to corrections of order $(t/\Delta)^2$, irrespective of the ratio t/V .

1. Canonical Transformation

Single particle tunneling on the honeycomb lattice couples the f -band to trimers, polarons and dipoles. The Schrieffer-Wolff transformation uses a canonical transformation $\mathcal{H}' = e^{iS}\mathcal{H}e^{-iS}$, with S Hermitian, to treat these couplings as an effective Hamiltonian that leaves the f -band invariant up to second order correction in t/Δ . This is achieved if S satisfies

$$[\mathcal{H}_0, iS] = \mathcal{H}_t, \quad (\text{A1})$$

as can be seen with the Baker-Campbell-Hausdorff formula. Under the assumption Eq. A1, we get

$$\mathcal{H}' = \mathcal{H}_0 + [iS, \mathcal{H}_t] + \mathcal{O}(\mathcal{H}_t S^2). \quad (\text{A2})$$

To find S , we follow Ref. [17] and split the tunneling Hamiltonian into a collection of operators $T_{p,M}$

$$\mathcal{H}_t = \sum_{p=\pm 1} \sum_{M=-2}^2 T_{p,M}, \quad (\text{A3})$$

where $T_{p,M}$ gathers all tunneling operations that change the number of occupied A sites by p and the number of occupied nearest neighbor pairs by M . The bounds for p and M are determined by the lattice geometry. With these definition, we can check that

$$S = -i \sum_{p,M} \frac{T_{p,M}}{MV + p\Delta}, \quad (\text{A4})$$

satisfies Eq. A1. Consider an eigenstate $|n\rangle$ of \mathcal{H}_0 with energy E_n . By definition $T_{p,M}|n\rangle$ is also an eigenstate of \mathcal{H}_0 with energy $E_n + (p\Delta + MV)$. As a consequence, we have

$$\begin{aligned} [\mathcal{H}_0, iS]|n\rangle &= \sum_{p,M} \frac{(E_n + p\Delta + VM)T_{p,M} - T_{p,M}E_n}{p\Delta + VM}|n\rangle \\ &= \sum_{p,M} T_{p,M}|n\rangle = \mathcal{H}_t|n\rangle. \end{aligned} \quad (\text{A5})$$

Finally, the relation $T_{p,M}^\dagger = T_{-p,-M}$ ensures the hermiticity of S . Plugging Eq. A4 into Eq. A2, we find the generic expression

$$\mathcal{H}' = \mathcal{H}_0 + \sum_{p,p',M,M'} \frac{[T_{p',M'}, T_{p,M}]}{M'V + p'\Delta} + \mathcal{O}\left(\frac{t^3}{\Delta^2}\right). \quad (\text{A6})$$

To evaluate the correcting terms of this last equation, we have noticed that all terms in S are smaller than t/Δ in magnitude.

2. Low energy projection

To describe the low-energy properties of our model, we project the obtained Hamiltonian onto the f -band which is well separated from other excitations by the charge transfer gap $\Delta \gg t$. This projection restricts the sum in Eq. A6 to cases where $p' = -p$ and $M' = -M$. Furthermore, the first operator acting on the states of the f -band should move an electron from an A to a B site, *i.e.* the rightmost $T_{p,M}$ must have $p, M \geq 0$. This gives

$$\mathcal{H}' \simeq \mathcal{H}_0 - \sum_{M=0,1,2} \frac{T_{-1,-M} T_{1,M}}{MV + \Delta}. \quad (\text{A7})$$

The three terms of the sum $M = 0, 1, 2$ gather all second order processes that respectively involve the virtual occupation of a trimer, a polaron and a dipole excitation (shown in Fig. 1). As expected from second order perturbation theory, these processes occur with rates

$$t_T = \frac{t^2}{\Delta}, \quad t_P = \frac{t^2}{V + \Delta}, \quad \text{and} \quad t_D = \frac{t^2}{2V + \Delta}, \quad (\text{A8})$$

that are inversely proportional to their energy difference with the f -band.

3. Simplification

To further simplify \mathcal{H}' , we isolate the contributions of Eq. A7 depending on the number of occupied neighbor of each A -site. In the following, we focus on a A -site at position r_0 and denote its three neighbors as r_1, r_2 and r_3 .

a. No neighboring fermions: If the A -site is surrounded by three empty sites, it can couple to three different dipole excitations in which the fermion at r_0 is moved on a B neighboring site. This provides an energy shift

$$\mathcal{H}_0 = -3t_D(1 - n_{r_1})(1 - n_{r_2})(1 - n_{r_3}). \quad (\text{A9})$$

b. One neighboring fermion: If the A -site has a neighboring fermion at position r_1 , it can couple to two polarons by hopping to either r_2 or r_3 . If the second tunneling process in Eq. A7 moves it back to r_0 , the process leads to an energy shift. On the contrary, if the fermion at r_1 replace the original one at r_0 , the process can be viewed as an effective tunneling of the r_1 -fermion on a neighboring B -site. Together, they give

$$\mathcal{H}_1 = -2t_P n_{r_1}(1 - n_{r_2})(1 - n_{r_3}) + t_P [f_{r_2}^\dagger (1 - n_{r_3}) + f_{r_3}^\dagger (1 - n_{r_2})] f_{r_1}. \quad (\text{A10})$$

Note that the tunneling terms come with a positive sign due to the anticommutation relation between fermions. Circular permutation of the indices (r_1, r_2, r_3) gives all other possible terms involving a polaron.

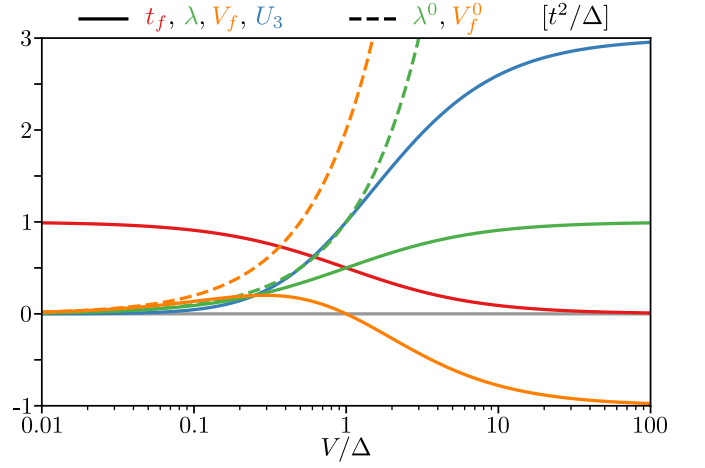


FIG. S1. Coefficients of the effective model Eq. 2 (full lines), and projection of the bare repulsion into the f -band (dashed) as a function of V/Δ .

c. Two neighboring fermions: Finally, if r_1 and r_2 both host a fermion, the system can only couple to a trimer excitation by moving the A electron to r_3 . The second tunneling process can either put this fermion back to r_0 , leading to an energy reduction, or put the ones at r_1 or r_2 at r_0 , giving a density-assisted tunneling term:

$$\mathcal{H}_1 = -t_T n_{r_1} n_{r_2} (1 - n_{r_3}) + t_T (f_{r_2}^\dagger n_{r_3} + f_{r_3}^\dagger n_{r_2}) f_{r_1}. \quad (\text{A11})$$

Again, circular permutation of the indices (r_1, r_2, r_3) gives all other possible terms involving a trimer.

Gathering the contributions of *a-b-c*, we obtain the effective Hamiltonian Eq. 2 where the coefficients originate from the processes outlined in Fig. 1. The single particle fermion tunneling only appears in Eq. A10 and therefore reads $t_f = t_P$. The correlated tunneling appears in Eqs. A11 and A10 with opposite signs: $\lambda = t_T - t_P$. Two-body and three-body interaction coefficients come from the three cases *a-b-c*. Carefully counting all terms, we find $V_f = -t_T + 4t_P - 3t_D$ and $U_3 = 3t_T - 6t_P + 3t_D$. These expressions are given in Eq. 3, and plotted against V/Δ in Fig. S1. For comparison (see text), we also show the results from the projection of the bare repulsion V into the f -band, valid when $V \ll \Delta$.

Appendix B: Solution of the two body problem

In this appendix, we solve the effective lattice model Eq. 2 for two fermions. To understand the competing roles of two-body interaction and correlated hopping, we first look at the quartic part of the Hamiltonian (Sec. B1). Then, we decouple the center of mass and relative motions of the two fermions (Sec. B2) and explain in more detail how the results presented in the main text were obtained (Sec. B3).

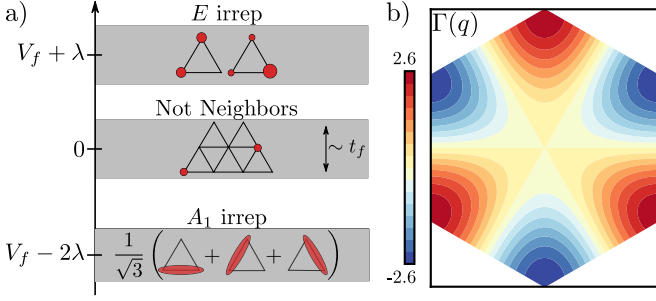


FIG. S2. a) The lowest energy subspace of $\mathcal{H}'_{\text{int}}$ is composed of bound states ($E_{A_1} = V_f - 2\lambda < 0$), which can be seen as dimers 'resonating' within an upper triangle of the B -lattice. b) Weight of the two-body ground state $\Gamma(q)$ in the limit $V \gg \Delta$. It is maximal in amplitude and opposite in sign at the K and K' points, underlying its valley-singlet nature.

1. 'Resonating' triangle

We start with the quadratic terms of our model

$$\mathcal{H}'_{\text{int}} = V_f \sum_{\langle i,j \rangle} n_i n_j + \lambda \sum_{(ijk) \in \Delta} (f_i^\dagger n_j f_k + P_{ijk}). \quad (\text{B1})$$

All states where the two electrons are not neighbors are zero energy eigenstates of this operator. The others have two doped charge on the same upper triangle, and can be divided into irreducible representations of C_{3v} . More precisely, there is a state in the identity representation A_1 and an E -doublet

$$\begin{aligned} |A_1, \mathbf{r}\rangle &= \frac{1}{\sqrt{3}} \left[f_{\mathbf{r}}^\dagger f_{\mathbf{r}+\mathbf{a}_1}^\dagger + f_{\mathbf{r}+\mathbf{a}_1}^\dagger f_{\mathbf{r}-\mathbf{a}_3}^\dagger + f_{\mathbf{r}-\mathbf{a}_3}^\dagger f_{\mathbf{r}}^\dagger \right] |n=1\rangle \\ |E, \mathbf{r}\rangle &= \frac{1}{\sqrt{6}} \left[f_{\mathbf{r}}^\dagger f_{\mathbf{r}+\mathbf{a}_1}^\dagger + f_{\mathbf{r}+\mathbf{a}_1}^\dagger f_{\mathbf{r}-\mathbf{a}_3}^\dagger - 2f_{\mathbf{r}-\mathbf{a}_3}^\dagger f_{\mathbf{r}}^\dagger \right] |n=1\rangle \\ |E', \mathbf{r}\rangle &= \frac{1}{\sqrt{2}} \left[f_{\mathbf{r}}^\dagger f_{\mathbf{r}+\mathbf{a}_1}^\dagger - f_{\mathbf{r}+\mathbf{a}_1}^\dagger f_{\mathbf{r}-\mathbf{a}_3}^\dagger \right] |n=1\rangle, \end{aligned} \quad (\text{B2})$$

with $|n=1\rangle$ the insulating state at unit filling, which also corresponds to the vacuum for the f operators. These three eigenstates of $\mathcal{H}'_{\text{int}}$ have energy

$$E_{A_1} = V_f - 2\lambda, \quad E_E = V_f + \lambda. \quad (\text{B3})$$

Because $V_f - 2\lambda < 0$, the lowest energy manifold is made of all states $\{|A_1, \mathbf{r}\rangle\}_{\mathbf{r} \in B}$ and has *negative* energy, corresponding to bound states. As mentioned in the main text, this binding energy solely comes from correlated hopping when $V \leq \Delta$, for which $V_f > 0$. These dimers have the f -wave symmetry described in the main text (see Fig. 2), and can be seen as dimers 'resonating' within an upper triangle as shown in Fig. S2.

This solution unveils the crucial role of correlated tunneling for pairing and gives an intuitive real-space picture for the bound pairs. It also allows to better understand the low energy continuum model Eq. 5. First, the coupling constant g is directly proportional to the energy $E_{A_1} < 0$. Moreover, it also gives a physical intuition for

the s -wave scattering between the two valleys. To see this, let's reintroduce the tunneling t_f in the lowest energy subspace $\{|A_1, \mathbf{r}\rangle\}_{\mathbf{r} \in B}$ to lift the degeneracy of the low energy manifold (this perturbative treatment of t_f is justified in the limit $V \gg \Delta$). The dispersion relation of the bound pairs $\varepsilon_{A_1}(k) = E_{A_1} - (2t_f/3) \sum_{j=1}^3 \cos(\mathbf{k} \cdot \mathbf{a}_j)$ has its minimum at the Γ point. The lowest energy state is

$$|\Gamma^{2e}\rangle = \frac{i}{\sqrt{3N_s}} \sum_{\mathbf{q} \in BZ} \Gamma(\mathbf{q}) f_{-\mathbf{q}}^\dagger f_{\mathbf{q}}^\dagger |n=1\rangle, \quad (\text{B4})$$

with $\Gamma(\mathbf{q}) = \sum_{j=1}^3 \sin(\mathbf{q} \cdot \mathbf{a}_j)$. The amplitude of the paired state $\Gamma(q)$ is maximal in magnitude near the K and K' points, as shown in Fig. S2. This confirms our intuition that the dominant scattering channel couples electrons with different isospin $\tau = \pm$ in s -wave to form valley singlets. While this argument gives an intuitive understanding of the dominant pairing interaction in our system, it can only be formally applied in the limit where $V \gg \Delta$ where the tunneling t_f can be treated as a perturbation to $\mathcal{H}'_{\text{int}}$.

2. Center of mass and relative motion

To solve the two-particle problem exactly, we now decouple the center of mass and relative motion of the two fermions. Taking all terms of Eq. 2 simultaneously into account, we obtain the results presented in Fig. 2, which also agree with the previous perturbative treatment of the previous section in the limit $V \gg \Delta$.

The Hilbert space with two fermions is spanned by the states

$$|r_1, r_2\rangle = f_{r_1}^\dagger f_{r_2}^\dagger |n=1\rangle. \quad (\text{B5})$$

Taking advantage of the translation invariance of the problem, we can introduce the center of mass momentum K and reorganize the Hilbert space with the Bloch-waves [44]

$$|\varphi(K, r)\rangle = \frac{1}{\sqrt{N_s}} \sum_R e^{i(K \cdot R)} |R, R+r\rangle. \quad (\text{B6})$$

Because $|r_2, r_1\rangle = -|r_1, r_2\rangle$, the state with opposite relative positions r describe the same physical state $|\varphi(K, -r)\rangle = -e^{i(K \cdot r)} |\varphi(K, r)\rangle$. To avoid double counting the states, we restrict our attentions to states with $(r \cdot \delta_1) \geq 0$. The action of the Hamiltonian in this new

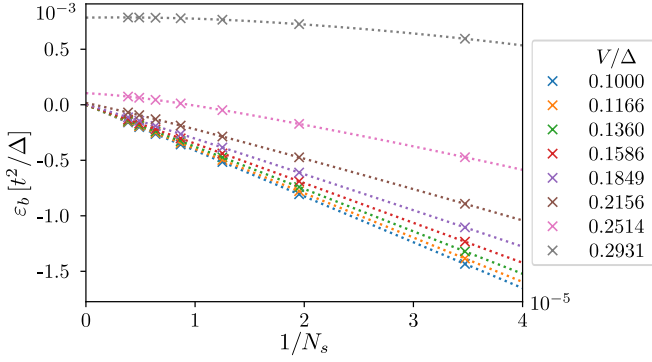


FIG. S3. Binding energy as a function of the inverse number of site. The linear behavior is extrapolated to $1/N_s \rightarrow 0$ for $V/\Delta < 0.25$ where extremely large system sizes are needed to accommodate the very weakly bound states (see Fig. 2).

basis can be directly computed

$$\begin{aligned} \mathcal{H}'|\varphi(K, r)\rangle = & \quad (B7) \\ & \sum_{\substack{j=1,2,3 \\ \epsilon=\pm}} t_f [1 + e^{i\epsilon(K \cdot a_j)}] |\varphi(K, r + \epsilon a_j)\rangle + V_f \delta_{r, \epsilon a_j} |\varphi(K, r)\rangle \\ & + \lambda \sum_j \delta_{r, a_j} |\varphi(K, -a_{j-1})\rangle + \delta_{r, -a_{j-1}} |\varphi(K, a_j)\rangle \\ & + \lambda \sum_j e^{-i(K \cdot a_{j+1})} \delta_{r, -a_j} |\varphi(K, a_{j-1})\rangle \\ & + \lambda \sum_j e^{i(K \cdot a_{j-1})} \delta_{r, a_j} |\varphi(K, -a_{j+1})\rangle. \end{aligned}$$

As expected from translation invariance, the state $|\varphi(K, r)\rangle$ only couple to states with the same center of mass momentum K . The tunneling on the lattice acts as an effective hopping term for the relative position r . The local interaction and correlated tunneling terms only changes this tight-binding Hamiltonian close to the origin for $r = a_j$ or $r = -a_j$ with $j = 1, 2, 3$. This tight binding Hamiltonian can be solved numerically for each center of mass momentum K . Its ground state always is at the Γ point, and reads $|\psi_{\text{bd}}\rangle = \sum_r \psi_{\text{bd}}(r) |\varphi(0, r)\rangle$. Its

energy yields the binding energy and bound state size

$$\xi_{\text{bd}} = \sqrt{\sum_r r^2 |\psi_{\text{bd}}(r)|^2}, \quad (B8)$$

in Fig. 2. Of course, accurate results can only be obtained when the system size exceeds the spread of the two-fermion bound state. In particular for $V/\Delta < 0.25$, the bound state size sharply increases and a more careful extraction of the energy is required.

3. Finite size scaling

We therefore focus on the regime $V/\Delta < 0.25$, and extract the two-body problem as a function of the inverse number of site in the system $1/N_s$ as shown in Fig. S3. Linear interpolation of these curves at $1/N_s = 0$ gives the values of the binding energy in the thermodynamic limit. The interpolated values are reported in Fig. 2. It is worth pointing out that we infer positive pair binding energy in the entire range $V/\Delta > 0$, in agreement with the continuum model.

Appendix C: Continuum model

1. Derivation

In this appendix, we derive the continuum model Eq. 5 in the limit of small doping concentration. Focusing on the physics near the K and K' pockets, and discarding all high energy fermionic degrees of freedom amounts to write the Fourier transform of the f -operators as

$$f_r = \frac{1}{\sqrt{N_s}} \sum_{\tau=\pm} \sum_{k, ka \ll 1} e^{-i[(\tau K + k) \cdot r]} \psi_{\tau, k}, \quad (C1)$$

with N_s the number of honeycomb unit cells. Total momentum conservation restricts the interaction terms to valley-preserving ones. They can be further decomposed as intra-valley interactions

$$H'_p = \frac{1}{2N_s} \sum_{k, q, q'} \left[\sum_{\tau} V_{k, q + \tau K} \psi_{\tau, q - k}^\dagger \psi_{\tau, q' + k}^\dagger \psi_{\tau, q'} \psi_{\tau, q} \right] \quad (C2)$$

and inter-valley interactions

$$H'_s = \frac{1}{2N_s} \sum_{k, q, q'} (V_{k, q + K} + V_{-k, q' - K} - V_{q' - q + k - 2K, q' - K} - V_{q - q' - k + 2K, q + K}) \psi_{+, q - k}^\dagger \psi_{-, q' + k}^\dagger \psi_{-, q'} \psi_{+, q}, \quad (C3)$$

which both depend on the momentum space representation of the quartic terms of Eq. 2:

$$V_{k, q} = \frac{V_f}{2t_f} \varepsilon(k) + \lambda \sum_{j=1}^3 e^{i(q \cdot a_j + k \cdot a_{j+1})} + e^{-i(q \cdot a_j + k \cdot a_{j-1})}. \quad (C4)$$

Due to the small momenta considered in our continuum theory, we can Taylor expand the previous expression

with the help of the relations

$$V_{k,q+\tau K} = 3(V_f - \lambda), \quad V_{k+2\tau K,q+\tau K} = -\frac{3}{2}V_f + 6\lambda, \quad (\text{C5})$$

which hold true up to $\mathcal{O}(k, q)$ corrections. This leading order approximation and the fermion anti-commutation relations show that intra-valley interactions $H'_p \simeq 0$ are negligible compared to inter-valley ones

$$H'_s = \frac{V_0}{2N_s} \sum_{k,q,q'} \psi_{+,q-k}^\dagger \psi_{-,q'+k}^\dagger \psi_{-,q'} \psi_{+,q}, \quad (\text{C6})$$

with $V_0 = 9(V_f - 2\lambda) = -9U_3$. Fourier transforming back to real-space and accounting for the Brillouin zone area, we obtain the effective interaction announced in Eq. 5:

$$\tilde{H}_{\text{int}} = g \int dx \psi_+^\dagger \psi_-^\dagger \psi_- \psi_+, \quad g = 2V_0 a^2 / 3. \quad (\text{C7})$$

2. Binding Energy

As a consistency check of our continuum model Eq. 5, we can determine the binding energy and compare it with the exact solution found in App. B. Using a T -matrix approach, the binding energy ε_b of the continuum theory is solution of the implicit equation [45]

$$\frac{1}{g} = - \int \frac{d^2 q}{(2\pi)^2} \frac{1}{\varepsilon_b + |q|^2/m}. \quad (\text{C8})$$

Going to polar coordinates $q = q_r e^{i\theta}$ and introducing the momentum UV cutoff Λ , we find

$$\frac{2\pi}{m|g|} = \int_0^\Lambda dq_r \frac{q_r}{q_r^2 + m\varepsilon_b}, \quad (\text{C9})$$

which can be integrated to obtain

$$\varepsilon_b = \frac{\Lambda^2}{m \left[e^{\frac{4\pi}{m|g|}} - 1 \right]}. \quad (\text{C10})$$

In order to fix the cutoff Λ , we can use our solution of the problem in the limit $V \gg \Delta$ of Sec. B 1, $\varepsilon_b = 3t^2/\Delta$. In that limit, Eq. C10 reduces to $\varepsilon_b \simeq (3\Lambda t)^2/(2\pi\Delta)$. Equating the two limits yields:

$$\Lambda = \sqrt{\frac{2\pi}{3a^2}} \simeq \frac{1.44720}{a}. \quad (\text{C11})$$

In Eq. 7, we have introduced the corresponding energy cutoff $\varepsilon_{\text{uv}} = \Lambda^2/m = \pi t_f = \pi W/9$.

Appendix D: Longer range interactions

In this appendix, we show evidence that longer range interactions neither destroy the effective pairing between

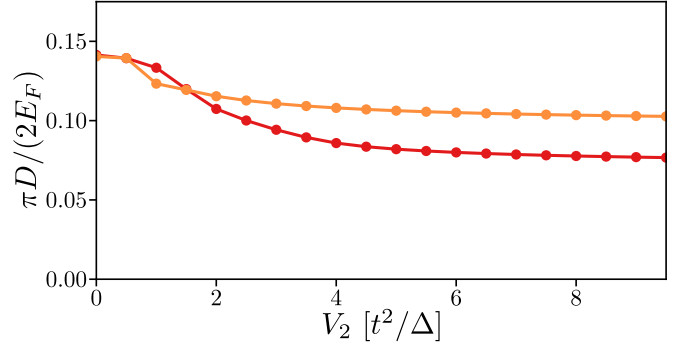


FIG. S4. Charge stiffness as a function of V_2 for 4 (orange) and 6 (red) particles in a 7×7 lattice with $V = 0.6\Delta$.

doped charges nor the superconducting phase described in the main text. We include next-nearest neighbor interactions $\mathcal{H}_2 = V_2 \sum_{\langle\langle r, r' \rangle\rangle} n_r n_{r'}$ in order to describe the tail of the fermion-fermion interaction.

The range of next-nearest interaction strength relevant for our work is $\Delta \sim V > V_2$. In that regime, the Schrieffer-Wolff transformation of App. A almost identically applies, up to two corrections. To first order, \mathcal{H}_2 introduces a direct interaction between electron in the f -band. To second order in t , it also changes the denominators of Eq. 3, which are determined by the new dipole, polaron and trimer energies:

$$\begin{aligned} E_D &= \Delta + 2V - 6V_2, \\ E_P &= E_f + \Delta + V - 5V_2, \\ E_T &= 2E_f + \Delta - 3V_2. \end{aligned} \quad (\text{D1})$$

For weak perturbations $V_2 \ll \Delta$, the second corrections can be safely discarded, and we obtain the same effective model as Eq. 2 with a two-body interaction strength

$$V'_f = V_2 + V_f. \quad (\text{D2})$$

At small doping, we can go to the continuum and the system is described by Eq. 5 with a modified coupling constant $g' = 3a^2(V'_f - 2\lambda)$ (compare with Eq. 6). When the additional interaction term is smaller than the largest pair binding energy ε_b of the original problem, *i.e.* $V_2 < 3t^2/\Delta$, we find that g' is negative when $V/\Delta \geq x_+$, where

$$x_+ = \frac{3v_2 + \sqrt{v_2(v_2 + 24)}}{4(3 - v_2)}, \quad v_2 = \frac{V_2\Delta}{t^2}. \quad (\text{D3})$$

In other words, at small δ , longer range interactions in the range $V_2 < 3t^2/\Delta$ only shifts the range of V/Δ where superconductivity is observed. For larger V_2 , the bound pairs break to avoid large next-nearest neighbor repulsion and the binding energy is always negative.

Even in that regime, the superconducting phase can reappear at larger doping concentrations. Indeed, if they are closely packed, the fermions of a pair do not decrease their energy by splitting apart because this send them

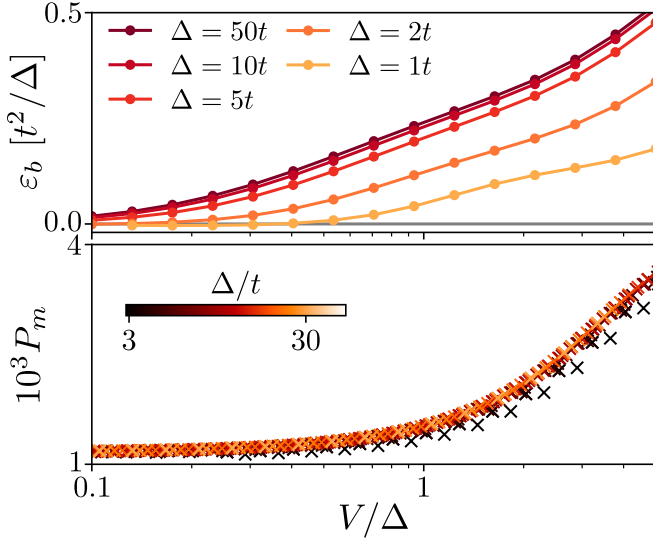


FIG. S5. The pair binding energy and pair correlation function for finite honeycomb lattice of 30 sites highlights the presence of two-body bound state and of a superconducting phase in the original model.

closer to all the other surrounding fermions in the system. We evidence the stability of the superconducting phase against V_2 at large doping with ED with 4 and 6 particles in a 7×7 lattice, thus at doping $\delta = 4/(7 \times 7) \simeq 8\%$ and $6/(7 \times 7) \simeq 12\%$, with $V = 0.6\Delta$. The charge stiffness extracted as a function of V_2 is shown in Fig. S4. Despite a slight decrease, the stiffness remains positive up to $V_2 = 10t^2/\Delta$. This gives support for the stability of the superconducting phase against longer range interactions at doping $\delta \sim 0.1 - 0.15$.

Finally, the regime $\Delta \sim V_2 \gg t$ has been extensively described in the in Ref. [15]. In that case, the trimer energy $E_T = 2E_f + \Delta - 3V_2$ can be resonant with the f -band. The presence of these preformed pairs in the Fermi sea of doped charges leads to superconductivity and pair-density waves. While the origin of pairs is different in that regime, strong V_2 interactions can still lead to superconductivity.

Appendix E: Pairing and superconductivity in the full-fledged model

We present ED results on the original model Eq. 1 in Fig. S5, which give further evidence for the presence of two-body bound pairs at finite doping above the $n = 1$ insulating state, and for the emergence of superconductivity in our model. The former is probed by the pair binding energy ε_b that we find, as in the main text, positive in the limit $t \ll \Delta$ for the entire range of V/Δ considered. For $\Delta \sim t$, we also observe a region with positive pair binding energy for sufficiently large V/Δ .

To investigate the superconducting correlations in the ground state of the doped $n = 1$ insulator, we calculate

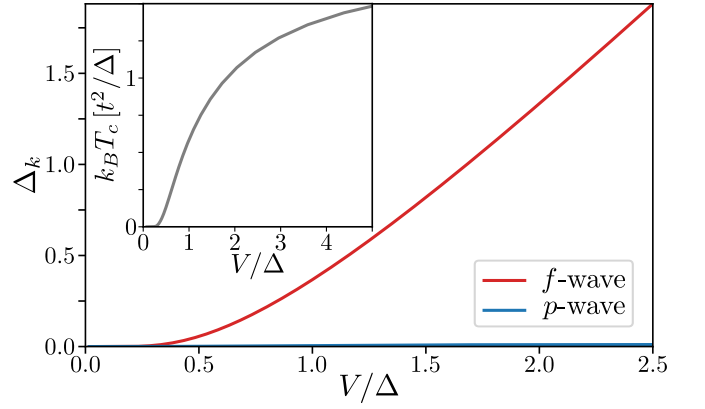


FIG. S6. Numerical solution Δ_k of the self-consistent gap equation for infinitesimal doping, decomposed into partial waves of p and f symmetry. The inset shows the self-consistent estimate of the critical temperature for $\delta = 0.05$, which almost perfectly match the exact formula Eq. 8.

the f -wave pair correlation function

$$P(r \in B) = \frac{1}{N_s} \sum_{x \in B} \langle \Delta_f^\dagger(r+x) \Delta_f(x) \rangle, \quad (\text{E1})$$

with $\Delta_f(x) = \sum_{j=1}^3 c_{x+\delta_j} c_x$. A superconducting state with f -wave symmetry is expected to exhibit a power-law decay of $P(r)$ with distance, and hence to have sizable correlations at large distances. For the largest accessible finite size clusters $N_s = 5 \times 3$, the maximum distance is achieved for $r_m = (2, 2)$. We denote the pair correlation function at this distance as $P_m = P(r_m)$. In Fig. S5, we show P_m as a function of the parameters V/Δ for several Δ/t . We observe large correlations in the perturbative limit $\Delta > 5t$ when $V/\Delta > 0.25$, where we indeed expect a strong superconducting order (see, for instance, Fig. 3). This direct manifestation of superconductivity gives strong evidence for the reliability of the predictions made from the effective model Eq. 2 and its mean-field solution detailed below in App. F.

Appendix F: Mean-field treatment

1. Dilute limit

We now carry out a self-consistent mean field treatment of the low-energy model Eq. 2 in the dilute limit, where three-body interaction terms are negligible. Going to Fourier space, the Hamiltonian becomes

$$\mathcal{H}' = \sum_k \varepsilon_k f_k^\dagger f_k + \frac{1}{N_s} \sum_{k,q,q'} V_{k,q} f_{q-k}^\dagger f_{q'+k}^\dagger f_{q'} f_q, \quad (\text{F1})$$

with $V_{k,q}$ defined in Eq. C4. Then we perform the mean-field substitution $f_{q'} f_q \simeq \delta_{q+q'} \langle f_{-q} f_q \rangle$. This replacement

leads to the following quadratic mean-field Hamiltonian

$$\mathcal{H}_{\text{MF}} = \frac{1}{2} \sum_k \begin{pmatrix} f_k^\dagger & f_{-k} \end{pmatrix} \begin{pmatrix} \xi_k & \Delta_k \\ \Delta_k^* & -\xi_k \end{pmatrix} \begin{pmatrix} f_k \\ f_{-k}^\dagger \end{pmatrix}, \quad (\text{F2})$$

$$\Delta_k = \frac{2}{N_s} \sum_q \text{Re}(V_{q-k,q}) \langle f_{-q} f_q \rangle,$$

where we have introduced a chemical potential μ and the short notation $\xi_k = \varepsilon_k - \mu$. We have also used the relation $V_{-k,-q} = V_{k,q}^*$. The quadratic Hamiltonian \mathcal{H}_{MF} is diagonalized as

$$\mathcal{H}_{\text{MF}} = \sum_k E_k \gamma_k^\dagger \gamma_k, \quad E_k = \sqrt{\xi_k^2 + |\Delta_k|^2}, \quad (\text{F3})$$

through the Bogoliubov transformation

$$\begin{pmatrix} f_k \\ f_{-k}^\dagger \end{pmatrix} = \begin{pmatrix} u_k & v_k \\ -v_k^* & u_k^* \end{pmatrix} \begin{pmatrix} \gamma_k \\ \gamma_{-k}^\dagger \end{pmatrix}, \quad (\text{F4})$$

$$u_k = \sqrt{\frac{1}{2} \left(1 + \frac{\xi_k}{E_k} \right)}, \quad v_k = -\frac{\Delta_k}{|\Delta_k|} \sqrt{\frac{1}{2} \left(1 - \frac{\xi_k}{E_k} \right)}.$$

The ground state of the system is annihilated by all quasi-particle operators γ_k and takes the form $|\Psi_{\text{BCS}}\rangle = \prod_k \gamma_k |n=1\rangle$. The order parameter Δ_k may now be computed self-consistently through the calculation of the correlators $\langle \Psi_{\text{BCS}} | f_{-q} f_q | \Psi_{\text{BCS}} \rangle$. This gives the so-called gap equation

$$\Delta_k = \frac{1}{N_s} \sum_q \text{Re}(V_{q-k,q} - V_{q+k,q}) u_q^* v_q$$

$$= \frac{1}{2N_s} \sum_q \text{Re}(V_{q+k,q} - V_{q-k,q}) \frac{\Delta_q}{E_q}. \quad (\text{F5})$$

Using the explicit form of $V_{k,q}$, this gap equation can be rewritten as

$$\Delta_k = \sum_{j=1}^3 u_j \sin(k \cdot a_j), \quad u_j = \frac{1}{N_s} \sum_q \phi_j(q) \frac{\Delta_q}{E_q}, \quad (\text{F6})$$

with

$$\phi_j(q) = -V_f \sin(qa_j) + \lambda [\sin(qa_{j+1}) + \sin(qa_{j-1})]. \quad (\text{F7})$$

Similarly, the mean particle number fixes the chemical potential μ through the relation

$$\delta = \frac{1}{2N_s} \sum_q \left(1 - \frac{\xi_q}{E_q} \right). \quad (\text{F8})$$

We solve the self-consistent gap equation numerically for infinitesimal doping and decompose the order parameter Δ_k into partial p and f -wave. The results are shown in Fig. S6. We observe that the self-consistent always has a solution, with a substantial gap for $\Delta/V > 0.25$. This provides another test of the continuum results of Fig. 3, where the critical temperature drastically rises near $\Delta/V = 0.25$. Furthermore, our mean-field solution exhibits a strong f -wave symmetry, which corroborates our exact two-fermion calculation (Fig. 2).

2. Critical temperature and three-body interactions

Including finite temperature effects to the previous analysis provides a way to determine the critical temperature T_c at which the pair are all broken by thermal fluctuation and $\Delta_k = 0$ [31]. This definition agrees with the superconducting temperature in the BCS limit of our model. Note that it does not capture the physics of the BKT transition, explaining why we obtain $k_B T_c \geq E_F/8$ in Fig. 3. Focusing on an order parameter with pure f -wave symmetry, the gap and number equations become

$$1 = \frac{1}{N_s} \sum_q \phi_j(q) \frac{\sum_p \sin(q \cdot a_p)}{|\xi_q|} \tanh \left(\frac{|\xi_q|}{2k_B T_c} \right) \quad (\text{F9a})$$

$$\delta = \frac{1}{2N_s} \sum_q \left[1 - \frac{\xi_q}{|\xi_q|} \tanh \left(\frac{|\xi_q|}{2k_B T_c} \right) \right]. \quad (\text{F9b})$$

We solve this implicit definition of T_c numerically. The results, presented in the inset of Fig. S6 for $\delta = 0.05$, show a sharp increase of T_c near $V = \Delta/4$. Excellent agreement is found with the continuum results of Fig. 3 in the small doping limit. For $\delta \geq 0.1$, the non-parabolicity of the dispersion relation leads to corrections to Eq. 8.

The three-body interaction terms of Eq. 2 can be partially reincorporated in Eq. F9 near T_c via the substitution

$$n_i n_j n_k \simeq \delta(n_i n_j + n_j n_k + n_i n_k) - \beta(f_i^\dagger n_j f_k + P_{ijk}),$$

where we have replace one quadratic operator by its expectation in the normal state $\langle n \rangle = \delta$ and $\langle f_k^\dagger f_i \rangle = \beta = N_s^{-1} \sum_k \cos(k \cdot a_1) f_{\text{FD}}(\xi_k)$ with f_{FD} the Fermi-Dirac distribution. This simply renormalizes the effective interaction V_f and correlated hopping strength

$$V_f' = V_f + \delta U_3, \quad \lambda' = \lambda - U_3 \beta, \quad (\text{F10})$$

which leads to a similar replacement of ϕ_j by

$$\phi_j'(q) = -V_f' \sin(qa_j) + \lambda' [\sin(qa_{j+1}) + \sin(qa_{j-1})] \quad (\text{F11})$$

in Eq. F9, as declared in the main text. The results shown in Fig. 3 are obtained with this substitution.

For fillings $\delta > 1/4$, we must rely on Eq. F9, which correctly describes the merging of the $\pm K$ pockets, while the two-flavor continuum model Eq. 5 assume them well-separated. At these doping concentrations, our calculations show that a superconducting state only appears for $V \geq 0.3\Delta$, in sharp contrast with the dilute regime where superconductivity extends to $V \ll \Delta$ (see Fig. 4). Another stark difference with the dilute limit is the presence of nodes of the superconducting gap located at the Fermi surface, which now encloses the Γ point.

Appendix G: ED evidence for nodal superconductor

We present more evidence of this nodal superconductor from ED of the effective model for $\delta > 1/4$. We focus on

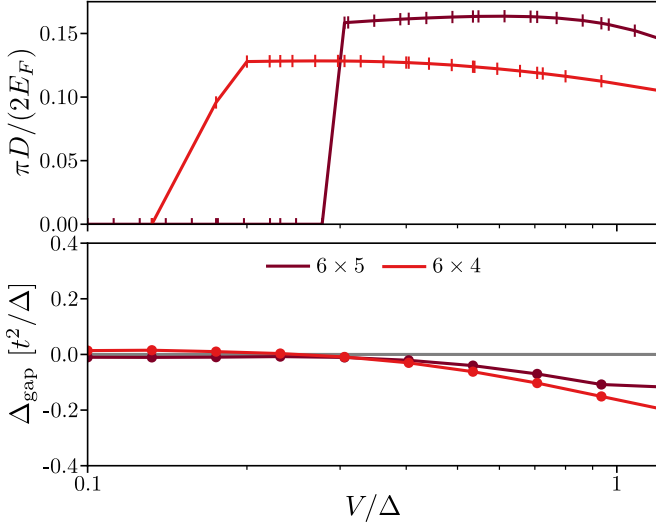


FIG. S7. Phase stiffness and superconducting gap obtained by ED of Eq. 8 for 6 (orange) and 8 (red) particles or more on 7×7 finite lattices.

lattices of size 7×7 with more than 6 particles, and extract the charge stiffness and the superconducting gap as in the main text. Our results are presented in Fig. S7. There, we observe that the system is not superconducting for $V \ll \Delta$, in agreement with the mean-field calculations of App. F. The transition to $D > 0$ occurs around $V = 0.2\Delta$, consistent with the mean-field value up to finite-size jitters. These observations comfort the presence of a superconducting phase at doping $\delta > 1/4$ and moderate V/Δ .

In the entire superconducting phase evidenced above, the superconducting gap Δ_{gap} is almost zero and decrease in magnitude with larger system size. This hints towards nodes of the superconducting gap at the Fermi energy, as expected from the Fermi surface topology and f -wave symmetry of the order parameter (see text).

Appendix H: Bosonic effective interactions and phase separation

In this appendix, we present our numerical results obtained outside of the superconducting region that we focus on in the main text. We have evaluated the charges stiffness of the ground state in a wide region of doping concentration and ratio V/Δ . Our results are presented in Fig. S8 for lattices with $L_1 \geq 7$ and $L_2 \geq 6$, which mitigate finite size effects. A white dashed line indicates where $\varepsilon_b = E_F$, and serves as an indicator to distinguish between the BCS and BEC limits predicted by the continuum model Eq. 5. As shown in the main text, the stiffness in the BCS region ($V < \Delta$) slowly increases but remains close to $E_F/8$, especially at small doping concentrations. In the BEC limit, we observe two different behaviors depending on the value of δ . First, the results

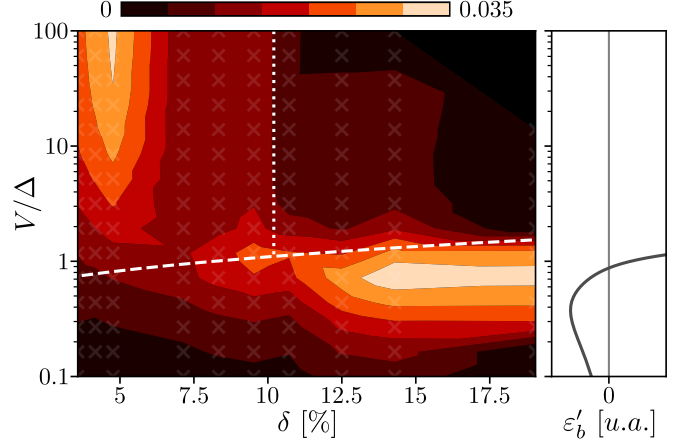


FIG. S8. Phase stiffness in a wider region of doping and ratio V/Δ . The white dashed line distinguishes between the BCS and BEC limits. The right panel shows the second binding energy. Its positivity indicates effective attractions between bosons deep in the BEC phase.

at $\delta < 10\%$ cannot reliably describe the thermodynamic behavior of the system as they were obtained for less than four particles. In that case, the small BEC is either a two-body or four-body bound state with a large effective mass. For larger doping, the lattice effects observed in the main text rule the physics and the charge stiffness drops down with increasing V/Δ . We observe that this diminution comes with a reduction of the many-body spectrum gap, until the ground state becomes highly degenerate for the $V > 70\Delta$.

To understand these features, we investigate the scattering properties of the local bosons in the $V \gg \Delta$ limit. To distinguish between attractive and repulsive interactions of pairs, we evaluate the second binding energy $\varepsilon'_b = 2E(2) - E(4) - E(0)$, which plays the same role as ε_b for the tightly bound pairs. The results presented to the right of Fig. S8, show a positive ε'_b for $V > \Delta$. This signals attractive interaction, which leads to the collapse of the quasi-BEC and to phase separation. The collapse of the BEC in favor of phase separation explains the large degeneracy observed for $V \gg \Delta$. The BEC collapse at large doping concentrations for $V > \Delta$ is also evidenced by a decay of the superconducting gap for $V > \Delta$, as shown in Fig. S9. Note that the points in the range $V < 1.2\Delta$ reproduce those of Fig. 4 in the main text.

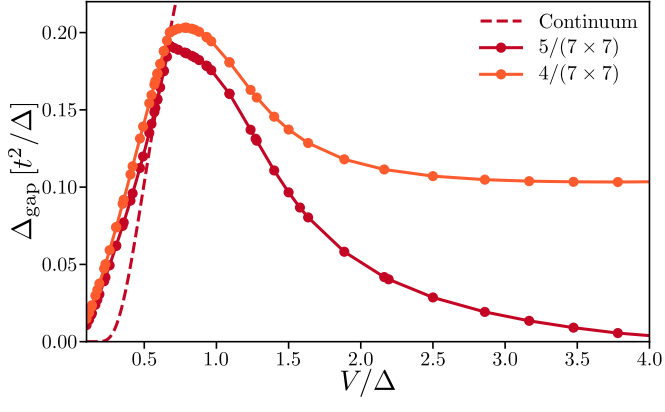


FIG. S9. Superconducting gap in a wider range of V/Δ . It reduces to almost zero at $V = 4\Delta$ for large doping concentrations.